

Improving percutaneous driveline performance by mechanical design modifications

Ekrem Ekici^{1*}, A. Alperen Koç² and Faleh AlThiyabi¹

¹*Interdisciplinary Research Center for Biosystems and Machines, King Fahd University of Petroleum and Minerals, Dhahran, 34464, Saudi Arabia.

²Department of Civil Engineering and Engineering Mechanics, Columbia University, New York City, 10027, NY, United States.

*Corresponding author(s). E-mail(s): ekrem.ekici@kfupm.edu.sa;

Contributing authors: ak5130@columbia.edu;
faleh.althiyabi@kfupm.edu.sa;

Abstract

The percutaneous drivelines serve as a biomaterial interface between the exterior component (controller) and the blood pump, transmitting signals and power for wired ventricular assist devices (VADs). For long-term support, the mechanical design of drivelines plays a key role in preventing driveline infections (DLIs) and VAD system malfunctions. However, the mechanical design of VAD drivelines remains understudied. In this study, we introduce a framework that combines experimental data with mathematical modeling to analyze the mechanical response of VAD drivelines. We perform characterization tests on two distinct drivelines (HeartWare and HM3) and conducted further bending experiments to investigate the properties of the multi-layered HM3 design. Using these experimental data, we develop and validate a mathematical model of bending behavior that explicitly captures the stick-slip mechanics and frictional interactions at the interfaces between material layers. A sensitivity analysis was then conducted to quantify the significance of both material and interfacial properties on the overall bending response. Among the parameters, the thickness of the outer insulating layer is most sensitive to the bending stiffness, highlighting a primary target for design optimization. These experimental and mathematical findings show how, mechanical and material properties of drivelines can be further modified, to improve the overall performance of VAD applications for heart failure patients.

Keywords: heart failure, ventricular assist devices, mechanical design, flexibility, bending modeling

This is a post-peer-review, pre-copyedit version of an article accepted for publication in *International Journal of Mechanics and Materials in Design*. Final authenticated version forthcoming at Springer Nature.

1 Introduction

An estimated 26 million people suffer from heart failure (HF), and the number of HF patients is showing an increasing trend worldwide [1, 2]. HF can be classified into two main types. The first, heart failure with reduced ejection fraction (HFrEF), is associated with the weakness of the heart muscle. The second, heart failure with preserved ejection fraction (HFpEF), is related to the impaired relaxation and filling of the heart without a primary pumping issue. To treat these conditions, ventricular assist devices (VADs) (Fig. 1a and Fig. 1d) are used to temporarily treat HF or provide long-term support. These devices contain an axial/centrifugal pump with sufficient power to provide additional circulatory support to the HF patient. The power and control signals for the rotor within VADs are transmitted through transcutaneous or percutaneous energy transfer systems. The wireless (transcutaneous) energy transfer systems are being studied extensively to eliminate cable-related problems. To this end, a wireless communication system was designed and its thermal behavior was studied in [3]. The designed wireless VAD system is compliant with thermal and EMF safety limits, ensuring the temperature rise remains below the 2°C in surrounding tissue. Although there are numerous ongoing clinical trials for wireless VADs [4], the long-term safety of these devices is still questionable and therefore requires further investigation.

On the other hand, wired VADs have been the primary choice for HF patients to this day. A percutaneous driveline/lead (Fig. 1b and Fig. 1e) is an indispensable part of wired VADs. It transmits power and communication signals between the blood pump and its controller. For the long-term success of VAD therapy, the mechanical design (Fig. 1c and Fig. 1f) and durability of the driveline are critical [5] to the overall system performance.

Driveline infections (DLIs), the most common type of infection [6] in VAD applications, may occur when the mechanical and thermal properties, as well as the biocompatibility of these cables are not well balanced. Considering the implanted section of the driveline, a notable study of 55 patients supported with the HeartMate II LVAD found that 69% of driveline damage occurred at the percutaneous portion of the cable, with an average time to damage of 1.9 years [7]. In addition, several mechanical factors affect the occurrence of DLIs, such as damaged silicone insulation [5], external [8] and internal wear / fractures [7], breakage in the cable sheath [9] and the externalization direction of the driveline [10]. These factors may cause redness, warmth, purulent discharge at the percutaneous entry site [11] and miscommunication between pump and controller. This miscommunication may then lead to severe pump malfunctions, eventually requiring further surgical procedures such as pump explantation and re-implantation [12]. The additional cost of this operation can vary between US\$178,000 and US\$230,000 [13, 14], reducing the financial efficiency of VAD therapy.

In order to increase the overall performance of VAD applications, several solutions have been proposed regarding drivelines. A C-shaped tunneling of the cable was suggested to minimize the risks caused by accidental pulling (e.g. by dropping the controller bag, falling out of the bed) [5]. The material and geometric properties of the driveline are also modifiable factors. Focusing on the former, driveline materials with lower torsional and bending stiffness are found to be correlated with lower DLI

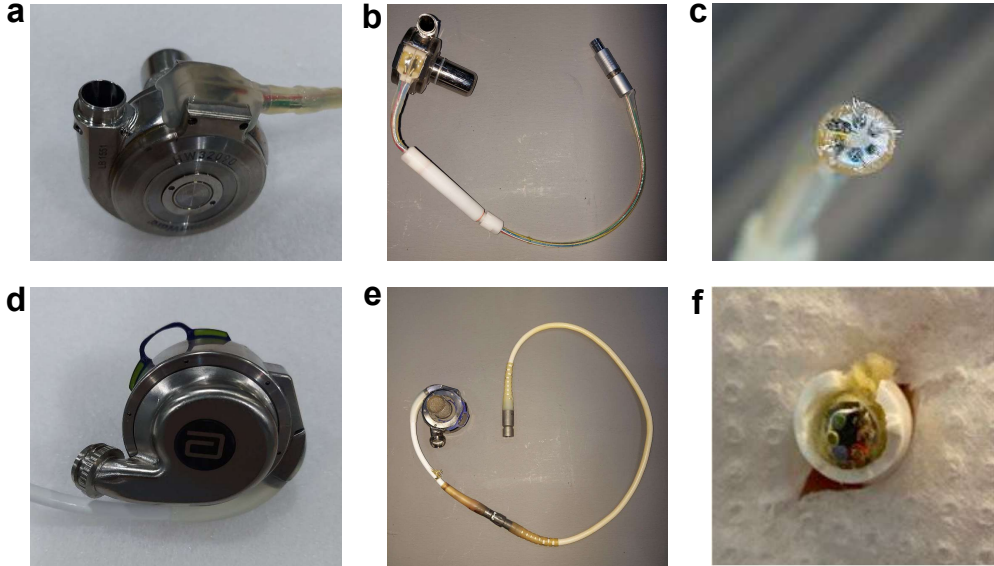


Fig. 1 Comparative views of the HeartWare VAD (top row) and HeartMate 3 (bottom row) VADs. The left, middle and right columns represent views for the pumps, drivelines, and a cross-section of the drivelines, respectively.

rates [15, 16]. During patient movement, stiff drivelines may increase the torque at the skin exit site, potentially causing pain and micro-trauma. Furthermore, stiff insulation materials can lead to cable breakage within the sheath, causing electrical disconnections and subsequent pump malfunction [17]. For these reasons, the HeartMate II driveline was changed using a softer material to minimize stress concentration and to prevent the breakage of the strain relief in the pump housing [5, 12]. Considering the driveline size, the overall diameter is found to be influential, with the hypothesis that smaller diameters may lead to smaller wound sites and less tissue disruption [15, 16] (See Appendix A)

Motivated by these findings, further analysis should be performed to improve the overall performance of drivelines for reduced DLI rates, increased patient comfort, and cost-effective VAD therapy. Therefore, experimental and mathematical modeling of driveline mechanics is vital to understand the bending and torsional stiffness of driveline designs.

In this paper, we present a comprehensive mechanical analysis aimed at deconstructing multilayered driveline bending behavior to inform future designs with improved overall VAD performance. First, we provide a general overview of existing driveline designs in Sec. 2. We then explain a standardized comparative bending test for the HeartMate 3 (HM3) and HeartWare VAD (HVAD) drivelines in Sec. 3. A detailed, layer-by-layer experimental analysis of the HM3 driveline is then conducted to reveal its non-additive composite behavior. To capture this complexity, a physics-based mathematical model from the literature is implemented and calibrated against

the experimental data in Sec. 4. Subsequently, the validated model is used to perform a quantitative sensitivity analysis (Sec. 5), identifying the key design parameters that govern flexural rigidity. Based on this parametric study, we provide a clear set of recommendations for improving mechanical designs of drivelines for reduced bending stiffness (in Sec. 6). Finally, we present our conclusions and potential future work in Sec. 7. In Appendix A, we present a weighted least squares regression analysis to reveal the importance of certain driveline mechanical features.

2 Existing driveline designs

The mechanical designs of contemporary drivelines represent a balance between mechanical flexibility, durability, overall diameter, and the electrical requirements for powering the pump without generating excessive heat. To achieve this balance, a common strategy across different VADs is the use of a layered, composite construction utilizing different materials. Hence, understanding the geometrical and material properties of drivelines requires an appreciation of the multi-material designs. To determine the internal geometry of the drivelines, we examined the cross-sectional areas of the HM3 and HVAD devices. The resulting layouts of these drivelines are presented in Fig. 2.

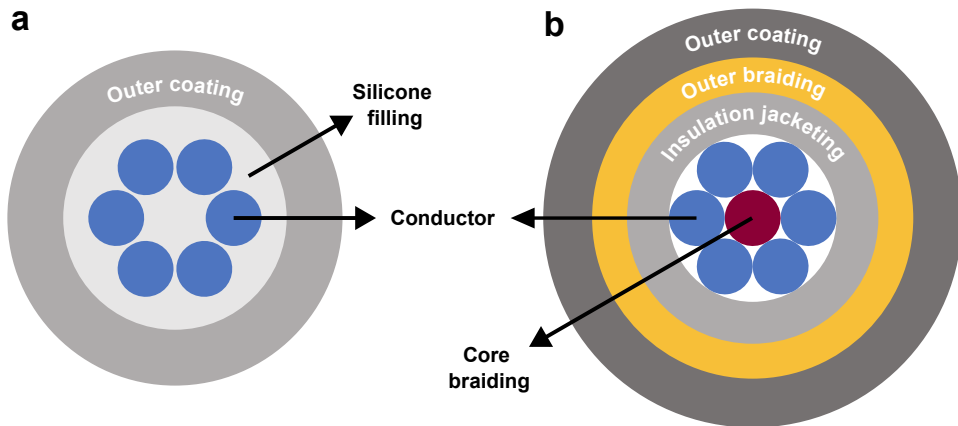


Fig. 2 Cross-sectional layouts of **a.** the HVAD driveline, composed of conductors within a silicone filling and a Pellethane outer coating, and **b.** the HM3 driveline, which features a polyethylene core, a polycarbonate-urethane (PCU) insulating jacket, aramid fiber braiding, and a silicone outer coating.

The HVAD driveline (Fig. 2a) utilizes a parallel conductor design, where six 30 American Wire Gauge (AWG) power conductors are arranged in a circular pattern. These conductors are embedded in a solid silicone filling for electrical insulation and positional stability. This entire assembly is then covered by a medical-grade Pellethane outer coating, which is designed to interface with biological tissue.

In contrast, the HM3 driveline (Fig. 2b) is built around a helical conductor arrangement. It utilizes six 30 AWG conductors for power and redundancy, which are helically stranded around a central braided polyethylene core that increases the tensile strength of the cable. The resulting wire bundle is encased in a polytetrafluoroethylene (PTFE) layer for low-friction movement, followed by a thermoplastic polycarbonate-urethane (PCU) insulating jacket. This jacket is then surrounded by an aramid fiber armor layer for mechanical reinforcement, and finally, the entire assembly is covered by an outer silicone coating for biocompatibility. In addition to the HM3 and HVAD drivelines, the mechanical features of some other drivelines are summarized in Table 1.

Table 1 Driveline properties including diameter, bending stiffness, and coating material. N/A stands for non-available features. All studies used a span length of 30 mm. For the bending measurements, the mid-span deflection is 12 mm in [16] and 5 mm in [15].

Device	Diameter (mm)	Bending stiffness (N)	Coating material	Reference
HeartMate II	6.0	≈4.52	Polyester velour	[15, 16, 18]
HeartMate 3	6.0	≈11.08	Woven polyester	[16, 18]
Duraheart	9.6	≈38	N/A	[15]
EVAHEART	9.7	≈54	N/A	[15]
Pellethane HVAD	4.8	≈15.55	Pellethane	[16]
Carbothane HVAD	4.8	≈8.50	Carbothane	[18, 19]

A key feature shared by these designs is the use of textured outer materials—such as woven polyester fabric or polyester velour. These coatings are specifically chosen to encourage tissue in-growth at the skin interface, which is critical for creating a stable biological seal against infection [20].

The *bending stiffness* values cited in studies represent the force required to achieve a pre-determined mid-span deflection (e.g., 12 mm [16] or 5 mm [15]). These values were obtained under three-point bending tests. All studies listed in Table 1 used a span length of 30 mm. However, a direct comparison of mechanical data across studies presents significant challenges. This approach is not mechanically representative, as drivelines exhibit highly nonlinear force-deflection behavior; the slope of the curve changes with deformation. Consequently, the measured force is not a normalized material property, but a test-specific value. This method of comparing stiffness can lead to contradictory rankings of driveline stiffness depending on the chosen maximum deflection. This discrepancy underscores that a single stiffness value is insufficient. In addition, small deflections are more clinically relevant due to the high frequency of small movements in daily patient activity. In order to provide a deeper understanding of the bending response and the contribution of individual layers, we follow a standardized experimental testing procedure, as explained in Sec. 3.

3 Experimental characterization

This section details the experimental methods used to characterize the bending properties of the HM3 and HVAD drivelines.

3.1 Bending test setup

To characterize the drivelines' response to bending, we designed a custom three-point bending test fixture compliant with the ISO 178:2019 standard [21]. The experimental setup is illustrated in Fig. 3. The 3D-printed supports were mounted on a 20 mm × 20 mm aluminum extrusion profile via screw holes, allowing the span between them to be adjusted. This adjustability is used to satisfy the depth-to-span ratio limitations specified in the standard, particularly because the two drivelines and different layers of HM3 tested have different diameters. A constant 1 : 16 depth-to-span ratio was used for all tests. This ratio was deliberately chosen to provide an optimal balance. The ratio is large enough to meet the slenderness requirements that minimize shear deformation. Meanwhile, it is also well-suited for our test setup to induce high curvatures without exceeding the physical deflection limits of the experimental setup. Rather than cutting samples, continuous segments of the drivelines were used. This setup creates overhanging sections on either side of the full driveline geometries during testing. 3D-printed plates were positioned at both sides (Fig. 3b) to eliminate these overhangs by supporting the remaining portions of the samples. As required by the standard, the supports (radii of 2 mm or 5 mm depending on the specimen depth) and the loading tip (radius of 5 mm) were 3D-printed using PETG filament with a 100% infill ratio to ensure rigidity during testing. A Lloyds Instruments LF Plus universal testing machine (AMETEK Inc., United States), equipped with a 100 N load cell, was used for testing. The applied force from the load cell and the resulting crosshead movement were recorded throughout the test. The crosshead speed was set to 2 mm/min for all tests as per the standard. The loading was applied in the vertical direction, aligned with gravity. The potential influence of sag due to the driveline's self-weight was evaluated. Based on a measured mass per unit length of 0.03 kg/m and the 96.0 mm test span, the maximum deflection from self-weight is calculated using beam theory to be approximately 0.06 mm. This value is less than 0.4% of the maximum deflection applied during testing and is therefore considered insignificant. The surrounding temperature was 22°C.

3.2 Experimental procedure and driveline results

Several portions of HVAD and HM3 drivelines were sliced, and the dimensions of each constituent layer were measured using a digital micrometer. The geometrical dimensions for the layers of both drivelines are provided in Table 2. Based on these values, the support radii and span dimensions for the HVAD and HM3 drivelines were calculated in accordance with the ISO 178:2019 standard [21].

Initial bending experiments were conducted on full driveline samples of both the HVAD and HM3. The HVAD driveline was tested with a span of 76.8 mm and a support radius (R_2) of 5 mm. The HM3 driveline was tested using a span of 96.0 mm with the same support radius. Because only a single driveline was available per device,

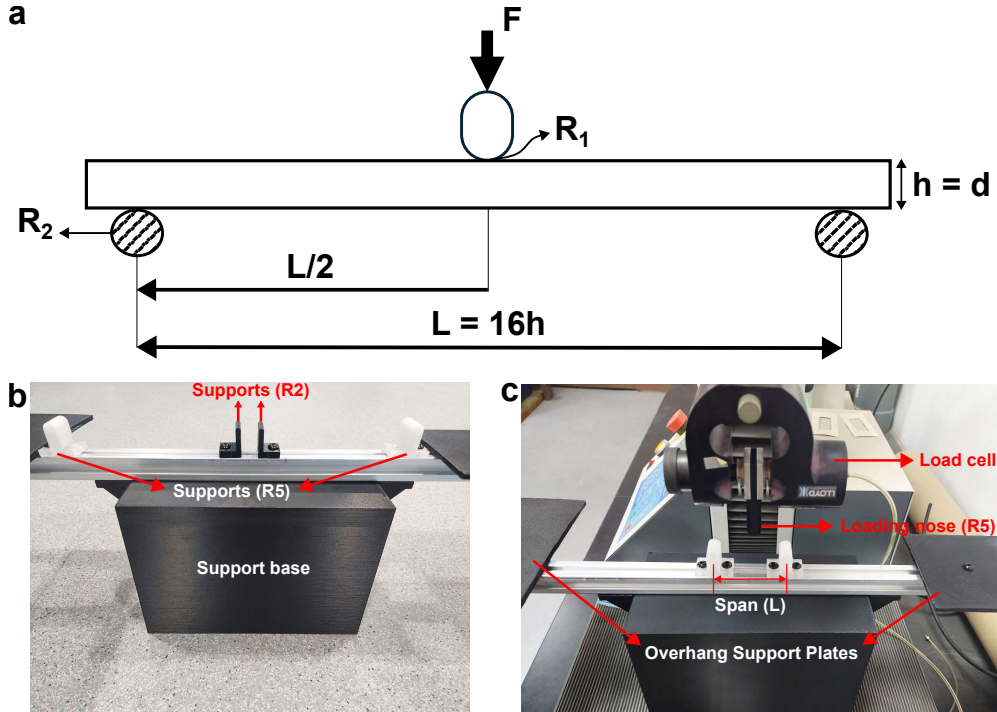


Fig. 3 The custom three-point bending test setup. **a.** Schematic of the test fixture, defining the support span (L), loading nose radius (R_1), and support radius (R_2). **b.** The 3D-printed base used to mount the adjustable supports with the supports with 5 mm radius (white) and 2mm radius (black). **c.** The fully assembled apparatus, configured with a 5 mm radius loading nose and 5 mm radius supports. The overhang support plates are also shown securing the driveline sample.

Table 2 Measured layer-by-layer dimensions of HVAD and HM3 drivelines.

Driveline	Component	Inner Diameter (mm)	Outer Diameter (mm)
HVAD	30 AWG conductor	-	0.8
	Silicone filling	-	3.2
	Pellethane coating	4.0	4.8
HM3	30 AWG conductor	-	0.8
	Core braiding	-	0.8
	Insulation jacketing	2.5	3.6
	Outer braiding	3.6	4.6
	Voven polyester coating	4.8	6.0

we repeated three experiments by sliding the samples by 10 mm as in [15]. Conducting three trials was deemed adequate, as our aim here is to compare the overall bending behaviors of drivelines. Hence, we do not use this data in the mathematical model. The raw force-displacement data, representing the mean of three tests per driveline, is presented in Fig. 4a.

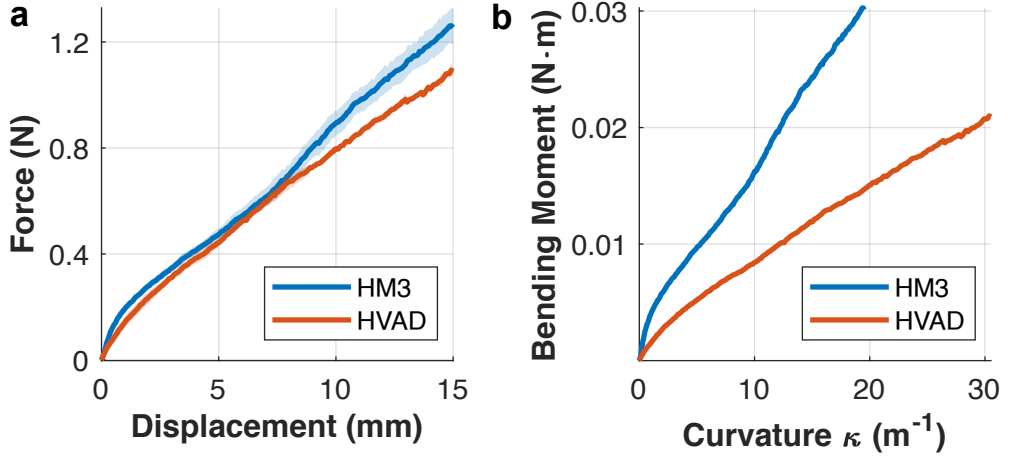


Fig. 4 Comparative bending analysis of HM3 and HVAD drivelines. **a.** Mean force-displacement curves from three experimental trials for each driveline, with the shaded regions representing the standard deviation. **b.** The corresponding moment-curvature relationship, calculated from the experimental data, shows the effective flexural rigidity of each driveline.

Both drivelines show a similar nonlinear trend with a continuously changing stiffness. While the curves appear close, a discernible difference is observed even in the small-deflection region. The mean responses separated by more than one standard deviation. This divergence becomes more apparent at deflections greater than 10 mm. However, raw force-displacement data can be misleading for direct interpretation (Sec 2). For example, in [16], Pellethane HVAD is reported to be stiffer than HM3 (Table 1). In our standardized bending experiments, we find the opposite to be true within the small deflection domain.

For correct and direct comparison of the intrinsic structural properties, it is essential to normalize the data. Therefore, the force-displacement results were converted into a moment-curvature relationship using small-deflection beam theory. For a three-point bending test, the maximum bending moment (M) at the center of the driveline and the corresponding curvature (κ) are calculated from the applied force (F) and mid-span deflection (δ) as $M = FL/4$ and $\kappa = 12\delta/L^2$, where L is the support span. The resulting plot (Fig. 4b) reveals a clear difference in mechanical response that was not apparent in the raw data. The HM3 driveline consistently shows higher effective flexural rigidity (EI) compared to the HVAD driveline within the entire range of displacements.

3.3 Deconstruction of HM3 Driveline Bending Behavior

Motivated by the findings in Sec. 3.2, we performed a detailed layer-by-layer analysis of the HM3 driveline to understand how each component contributes to the overall flexural rigidity. These tests were conducted using the same three-point bending setup described in Sec. 3.1, maintaining the 1:16 depth-to-span ratio for all layers and sub-assemblies. In order to obtain greater statistical rigor for more elaborate mathematical

modeling (Sec. 4), we increased the number of trials to six. We used single available layers for core braiding and sub-assemblies, and test them by sliding by 10 mm as in Sec. 3.2. However, we tested six individual 30 AWG wires of the HM3 driveline. The 30 AWG conductor and core braiding were tested as isolated single components, while the other configurations were tested as progressively larger sub-assemblies, as tabulated in Table 3. The experimental parameters were adjusted according to the geometry of each sample.

Table 3 Span and support radii (R_2) used for three-point bending tests of individual HM3 layers in accordance with the ISO 178:2019.

HM3 Layer	Span (mm)	R_2 (mm)
30 AWG conductor	12.8	2
Core braiding	12.8	2
6 wire + core braiding	40.0	2
6 wire + core braiding + insulation	57.6	5
6 wire + core braiding + insulation + outer braiding	76.8	5

As in Sec. 3.2, the recorded force-deflection data for each layer was converted into an effective flexural rigidity (EI) versus curvature relationship. Fig. 5a provides a clear visual hierarchy of the effective flexural rigidity (EI) of each component and sub-assembly. As expected, the addition of each successive layer results in a progressive increase in the overall bending stiffness, illustrating how each component contributes to the final mechanical properties. However, the magnitude of this increase is not constant for each subsequent layer. The relationship between the layers is more complex than a simple summation.

To further investigate the composite nature of the 7-wire strand (six 30 AWG conductors wrapped around the core braiding), its experimentally measured response was compared against two fundamental theoretical bounds (Fig. 5b). The lower bound, analogous to a Reuss estimate, represents the ideal case of frictionless slip between components, where the total flexural rigidity is the linear sum of the individual rigidities: $EI_{lower} = EI_{core} + 6 \times EI_{awg}$, where subscripts *awg* and *core* denote the single 30 AWG wire and core braiding, respectively. The upper bound, analogous to a Voigt estimate, represents the case of perfect bonding (infinite friction), where the assembly acts as a single monolithic beam. Its flexural rigidity (EI_{upper}) was calculated using the parallel axis theorem. Assuming a homogenized effective modulus (E_{awg}) and area (A_{awg}) for the outer wires, the total rigidity is the sum of the core's rigidity and the rigidity of the six outer wires, including their transfer term:

$$EI_{upper} = EI_{core} + \sum_{i=1}^6 (EI_{awg} + E_{awg} A_{awg} d_i^2), \quad (1)$$

where d_i is the vertical distance of the i -th wire's centroid from the neutral axis of the assembly. For a hexagonal packing geometry with wire radius r , the distances for the

four wires not on the neutral axis are $d = 2r \sin(60^\circ) = r\sqrt{3}$. The total contribution from the transfer term for these four wires is $4 \times E_{awg} A_{awg} (r\sqrt{3})^2$. Given that for a circular cross-section, $A = \pi r^2$ and $I = \pi r^4/4$, we can express the area as $A = 4I/r^2$. The transfer term for the four wires simplifies to $4 \times E_{awg} (4I_{awg}/r^2)(3r^2) = 48 \times EI_{awg}$. The final expression for the upper bound is therefore:

$$EI_{upper} = EI_{core} + 6 \times EI_{awg} + 48 \times EI_{awg} = EI_{core} + 54 \times EI_{awg}. \quad (2)$$

As illustrated in Fig. 5b, the experimentally derived curve lies distinctly between these two limits, demonstrating that the overall response is governed by complex, non-linear frictional interactions. This comparison is intended to highlight the non-additive nature of the composite structure and motivate the need for a more sophisticated analysis. Advanced homogenization techniques, such as numerical multiscale modeling, provide powerful methods for deriving the effective properties of such complex composites [22, 23]. However, the significant deviation from these simple bounds justifies the development of the specific, physics-based stick-slip model presented in Sec. 4.

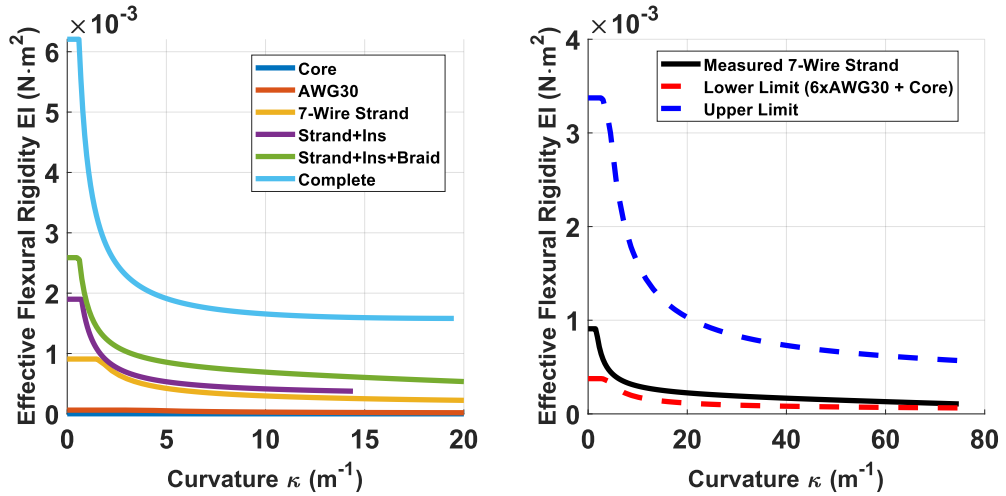


Fig. 5 Deconstruction of HM3 driveline bending mechanics. **a.** Effective flexural rigidity-curvature relationships for individual layers and sub-assemblies of the HM3 driveline. **b.** Comparison of the experimentally measured 7-wire strand response against its theoretical lower bound (simple summation) and upper bound (monolithic beam) in terms of effective flexural rigidity.

4 Mathematical bending modelling

In this section, we analyze the mechanical behavior of the multilayered driveline HM3 with mathematical modeling. We adapted the analytical framework for the bending of helically stranded wires presented by Vemula et al. [24]. We consider small deformations to mimic more prevalent daily patient activities (clarified in Sec. 2). Therefore,

the large deflection and plasticity formulations of the original model were not implemented. Our study deliberately focuses the modeling effort on the driveline's inner core (up to the insulation jacketing, Fig. 2b) to isolate and validate the dominant mechanical nonlinearity: the stick-slip friction between the helically stranded wires. This focused scope is justified as the outer aramid armor is engineered primarily for cut resistance, contributing minimally to bending stiffness. The modeled assembly consists of a 7-wire strand—a central core helically wrapped by six signal cables—with an intervening low-friction Teflon layer. Our methodology uses a hierarchical approach, first characterizing the bending behavior of the individual 30 AWG signal cables experimentally to serve as a validated input for the larger assembly model.

4.1 30 AWG bending characterization

A continuous, piecewise function was fitted to the average of 30 AWG bending data to model the characteristic stick-slip response, a key component of the cable's nonlinear behavior. The function defines the applied force F (N) as a function of deflection δ (m). It consists of an initial linear region followed by a quadratic region:

$$F(\delta) = \begin{cases} 874.68 \cdot \delta & \text{if } \delta \leq 1 \times 10^{-4} \\ -27452.31 \cdot \delta^2 + 203.67 \cdot \delta + 0.07 & \text{if } \delta > 1 \times 10^{-4} \end{cases} \quad (3)$$

The effective bending stiffness, EI_{awg} , was derived from the continuous force-deflection curve using the relationships for moment and curvature defined in Section 3.2. Combining these relationships ($EI = M/\kappa$) provides the effective bending stiffness as a function of deflection:

$$EI(\delta) = \frac{F(\delta)L^3}{48\delta}, \quad (4)$$

where $F(\delta)$ is the piecewise function defined previously, and L is the test span length. The resulting force curve (Fig. 6a) and the derived bending stiffness profile (Fig. 6b) are shown and serve as the final homogenized input for the larger driveline model. This method allows for an accurate representation of the cable's nonlinear behavior without modeling its internal complexity.

4.2 Helical 7-wire cable

With the properties of the individual signal cables defined, we model the behavior of the complete 7-wire strand. The overall bending response of the driveline is governed by the stick-slip kinematics between the seven constituent cables and the insulating jacketing. The model, based on [24], uses Euler-Bernoulli beam theory for the overall driveline bending. Initially, in the "stick" state, all seven cables bend as a single, cohesive unit. The axial strain (ϵ) under pure bending in any given cable is a function of the driveline's overall curvature (κ_w), the cable's radial position (r_q), its angular position ($\theta_{p,q}$), and its lay angle (α_q):

$$\epsilon_{p,q} = \kappa_w r_q \sin \theta_{p,q} \cos^2 \alpha_q. \quad (5)$$

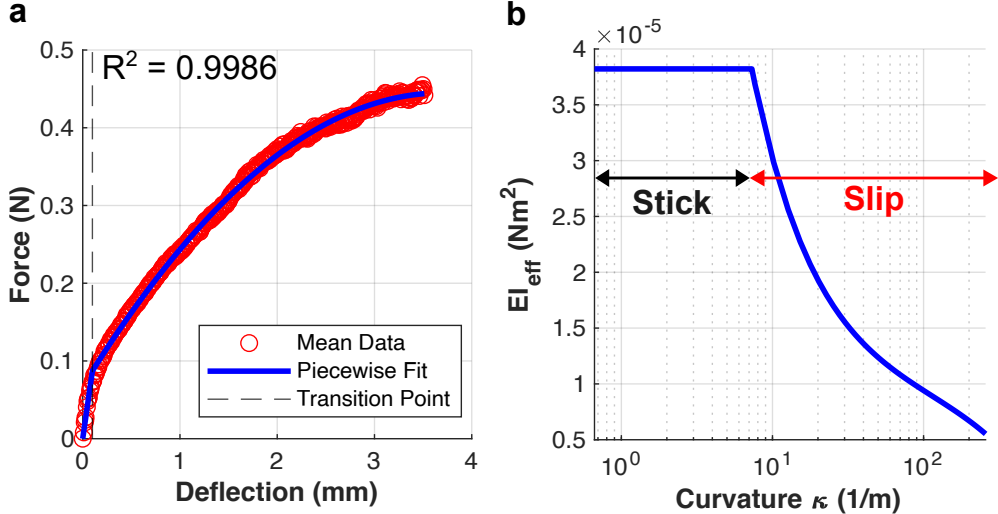


Fig. 6 Bending characterization of a single 30 AWG wire of HM3 driveline. **a.** Force-deflection comparison of the experimental mean data and the fitted piecewise curve, **b.** Effective bending stiffness vs curvature of the fitted model.

The corresponding axial force (T) in the cable is the product of this strain and the cable's axial rigidity:

$$T_{p,q} = EA_{cable}\kappa_w r_q \sin \theta_{p,q} \cos^2 \alpha_q. \quad (6)$$

As bending increases, the induced axial forces overcome the static friction between adjacent cables, initiating a "slip" state where the cables slide relative to one another. The model uses the Amontons-Coulomb friction law to define the maximum sustainable frictional force for each of the six outer signal cables. For our specific 7-wire strand, the general model simplifies significantly. The subscripts p and q refer to the cable number within a layer and the layer number, respectively. Here, we are only concerned with the single layer of six outer cables ($q = 1$, $p = 1 : 6$).

The maximum frictional force ($F_{p,1}$) for a given outer cable p is calculated as:

$$F_{p,1} = (\exp(\mu_s \sin \alpha_1 \theta_{p,1}) - 1) \frac{(\mu_p + \mu_s) F_{rad}}{\mu_s \sin \alpha_1} \quad (7)$$

where μ_s is the inter-cable friction coefficient (between outer cables and the core), μ_p is the friction coefficient between the outer cables and the insulation jacket, α_1 is the lay angle of the outer cables, $\theta_{p,1}$ is the angular position of the p th cable, and F_{rad} is the radial force from the insulation jacket.

The actual axial force (F_{axial}) in each outer cable is therefore the minimum of the force required to maintain the stick condition and this maximum sustainable frictional force:

$$F_{axial} = \min(T_{p,1}, F_{p,1}). \quad (8)$$

The total bending moment (M) of the cable is the sum of the bending resistance of the individual cables and the moment generated by the axial forces within them:

$$M = \sum (EI_{\text{cable}})\kappa_w + EI_{\text{ins}}\kappa_w + \sum (F_{\text{axial}} \cdot r_q \sin \theta_{p,q}), \quad (9)$$

where EI_{cable} is the bending stiffness of a single helically wrapped 30 AWG cable, and EI_{ins} is the bending stiffness of the outer insulation jacket of the complete driveline. EI_{cable} is calculated as:

$$EI_{\text{cable}} = \frac{\cos(\alpha_q)}{2} EI_s \left(1 + \cos^2 \alpha_q + \frac{\sin \alpha_q}{1 + v_s} \right), \quad (10)$$

where EI_s is the experimentally derived bending stiffness of a straight 30 AWG cable, v_s is the Poisson's ratio of the cable, and α_q is the helix angle of the cable wrap.

4.3 Model calibration

In the established mathematical model, the intricate frictional interactions and radial pressures within the driveline are represented by three effective parameters: the inter-cable friction (μ_s), the cable-jacket friction (μ_p), and the radial force (F_{rad}). These parameters do not represent simple material properties but rather the homogenized effect of complex physical phenomena. For instance, μ_p is an effective coefficient that incorporates the combined frictional behavior at the cable-jacket interface, including the influence of the thin Teflon layer. As these parameters encapsulate system-level behaviors that are impractical to measure directly, they must be determined by calibrating the model's output against the experimental force-deflection data of the complete 7-wire assembly.

To identify a robust set of these parameters and reduce the dependency on an arbitrary initial guess, a global optimization approach was employed. Specifically, MATLAB's *GlobalSearch* routine was used. It runs a local solver, *fmincon*, repeatedly from various start points across the parameter space.

The optimization objective was to minimize the Sum of Squared Errors (SSE) between the model's predicted force and the mean force-deflection curve derived from the three experimental trials. The optimization problem is formulated as:

$$\begin{aligned} \min \quad & \text{SSE} = \sum_{i=1}^n (F_{\text{model}}(\delta_i) - \bar{F}_{\text{exp}}(\delta_i))^2 \\ \text{subject to} \quad & \begin{cases} 0.1 \leq \mu_s \leq 0.7 \\ 0.1 \leq \mu_p \leq 0.7 \\ 0.0 < F_{\text{rad}} \end{cases} \end{aligned} \quad (11)$$

where $F_{\text{model}}(\delta_i)$ is the model's predicted force at the i -th displacement point, and $\bar{F}_{\text{exp}}(\delta_i)$ is the mean experimental force at that same displacement. As shown in (11), the friction coefficients (μ_s, μ_p) were constrained to be positive to maintain physical realism. Their minimum and maximum limits were set to be 0.1 and 0.7, respectively.

This range is found to be typical for representing friction within stranded electrical wires [25, 26]. In addition, the radial force (F_{rad}) must be positive as the shrink-fit insulation jacket is expected to exert a compressive force on the internal cable bundle.

It was observed that repeated executions of the global search, even with extensive run times, converged to different parameter sets that all yielded nearly identical, high-quality fits ($R^2 = 0.9939$) to the experimental data. This outcome is typical for complex physical models where strong parameter correlations create a vast solution space with multiple, near-optimal local minima. Therefore, the goal of this calibration is not to assert the discovery of a single, unique parameter set. Instead, we aim to demonstrate a physically plausible set which accurately reproduces the system's macroscopic behavior as in [24]. A more rigorous investigation into parameter identification and the quantification of their uncertainties is beyond the scope of this paper.

The final calibrated parameters reported represent one such high-fidelity solution, with the quality of fit quantified by the coefficient of determination (R^2) in Table 4.

Table 4 Model fit performance and its calibrated parameters.

Parameter	Initial Value	Range	Optimized Value
μ_s	0.25	0.1 - 0.7	0.01
μ_p	0.1	0.1 - 0.7	0.46
F_{rad} (N)	0.5	0.03-0.24	0.11
R^2	0.8832	0.9939	0.9939

The success of this calibration is visually demonstrated in Fig 7. The figure presents the optimized model's effective bending stiffness profile, which drives the simulation. More importantly, it shows the final force-deflection curve, where the optimized model's prediction aligns closely with the mean experimental data and falls well within the 90% confidence interval. This close alignment also visually confirms the high R^2 value reported in Table 4. This validation approach, which compares a physics-based model against macroscopic experimental data, is consistent with the established methodology for analyzing such systems [27–30]. It should also be noted that the implemented model does not account for the effect of temperature changes on bending stiffness EI . This omission represents a potential limitation of the study's findings, as the model parameters were calibrated at an ambient temperature of 22°C, rather than an average body temperature of 36.5°C.

4.4 Interaction between model parameters

Although we do not have an optimal solution for this problem, it is still informative to understand the effect of parameters on the bending behavior. We would like to further reveal the inter-parameter relationships for our nonlinear model. For this, we sweep the specified ranges for the friction coefficients (μ_s and μ_p) as in Eq. (11), then

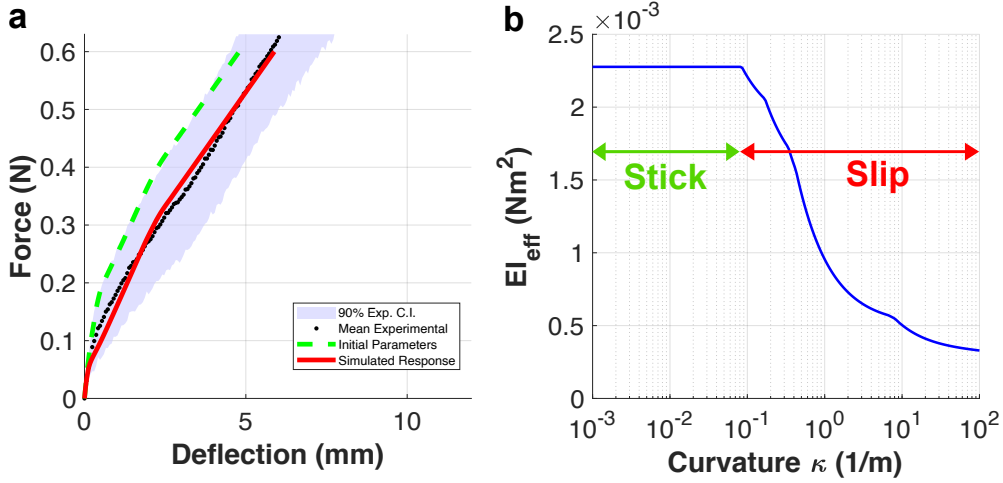


Fig. 7 Final results of the calibrated model. **a.** Comparison of the model’s force-deflection prediction against the mean experimental data. The shaded region represents the 90% confidence interval of the experimental trials. **b.** The effective bending stiffness (EI_{eff}) versus curvature (κ_w) for the final optimized assembly model.

we find the optimum radial force (F_{rad}) giving the predefined fit ($R^2 = 0.9939$) with the data. The results are presented as a contour plot in Fig. 8.

The interaction between friction coefficients μ_p and μ_s is linear, as one increases, the other must decrease to maintain the same fit. However, this trade-off is not symmetrical. For example, at a constant radial force of (F_{rad}) 0.08N, when μ_s is at its lower bound (0.01), μ_p is 0.54. Conversely, when μ_s is at its lower bound, the μ_s becomes 0.46. Unsurprisingly, the radial force increases as the friction coefficients decrease, reaching its maximum when $\mu_s = \mu_p = 0.1$. The model’s sensitivity is highly nonlinear, with the radial force changing along the diagonal from bottom-left to top-right, but this change is most drastic in the low-friction-coefficient region. This is due to the nonlinearity in the mathematical model, which must compensate to maintain the predefined fit with the experimental data.

5 Sensitivity of design parameters

Using the validated mathematical model, a sensitivity analysis was performed to identify which design parameters have the most significant influence on the overall bending stiffness of the driveline. A one-at-a-time (OAT) approach was used, in which each parameter was varied above and below its calibrated baseline value (Table 4) while all other parameters were kept constant. The parameter ranges in the OAT analysis were selected to represent plausible physical, material, and manufacturing limits rather than a uniform percentage-based variation. This approach allows for a more realistic exploration of the engineering design space. For instance, the lay angle range (5° to 45°) was chosen to span from a loose, near-parallel wrap to the practical upper limit for a tight helical structure. Similarly, the friction coefficient range (0.05 to 0.50)

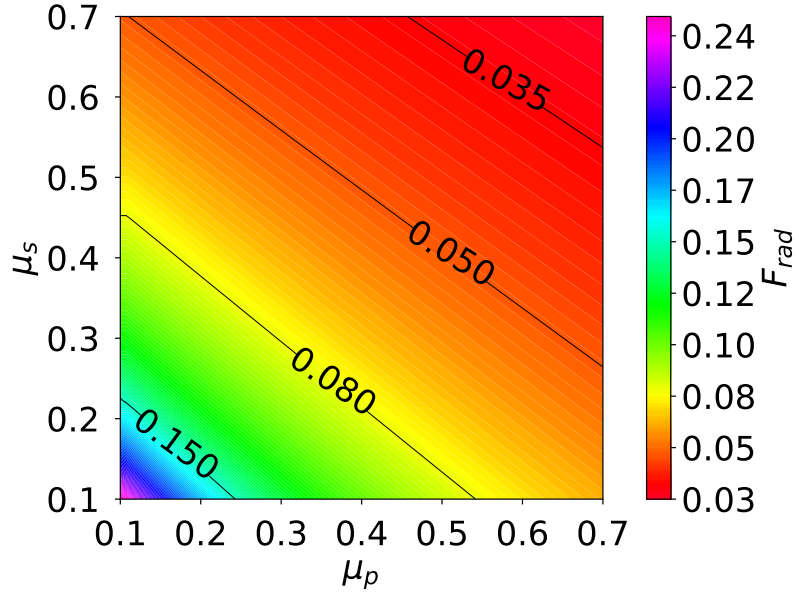


Fig. 8 Parameter sweep to reveal interactions between parameters within the nonlinear model. The horizontal and vertical axes represent the friction coefficients μ_p and μ_s respectively, while the colorbar shows the radial force values. The black lines show iso-lines representing the constant F_{rad} .

reflects the potential material behavior from its pristine, low-friction state to a worn, higher-friction state over the device's lifetime. The parameters, their baseline, low variant, and high variant values are summarized in Table 5. Furthermore, the selected ranges for the interfacial properties (μ_s , μ_p , and F_{rad}) are consistent with the optimal solution space identified during model calibration (Fig. 8).

Table 5 Parameters, baseline values, and ranges used in the sensitivity analysis.

Parameter	Units	Symbol	Baseline Value	Low Variant	High Variant
Insulation modulus	MPa	E_{ins}	40	20	60
Insulation thickness	mm	t_{ins}	0.6	0.15	1.05
Lay angle	°	α	10.5	5	45
Inter-cable friction	—	μ_s	0.20	0.05	0.50
Cable-jacket friction	—	μ_p	0.20	0.05	0.50
Poisson's ratio	—	ν_s	0.30	0.15	0.45
Radial force	N	F_{rad}	0.1	0.05	0.3

The qualitative effect of these variations on the force-deflection curve is shown in Fig. 9, providing a visual guide to each parameter's influence. The geometric and

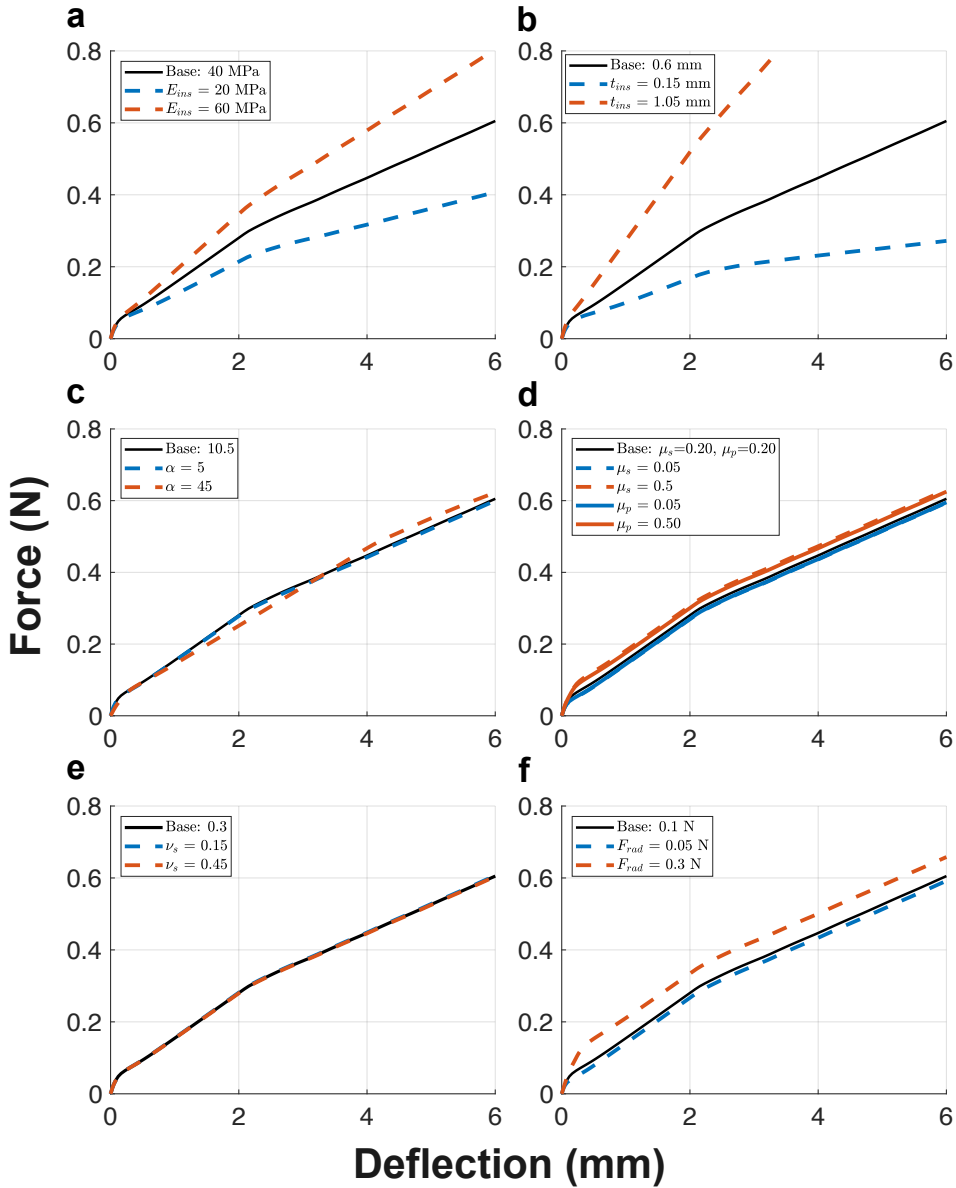


Fig. 9 Results of the one-at-a-time sensitivity analysis, showing the effect of varying key design parameters on the model's predicted force-deflection curve: **a.** Young's modulus of the insulation layer, **b.** thickness of the insulation layer, **c.** lay angle of the 30 AWG cable, **d.** inter-cable and cable-jacket friction coefficients, **e.** Poisson's of the 30 AWG cable, **f.** radial force applied by the insulation layer. The solid black line in each subplot represents the baseline response using the baseline parameters from Table 5.

material properties of the insulation jacket—its thickness (t_{ins}) and Young's modulus (E_{ins})—are the most dominant parameters (Fig. 9a and Fig. 9b). They affect both the slip and stick regions. On the other hand, the interfacial properties—the radial force (F_{rad}) and the friction coefficients (μ_s , μ_p)—primarily govern the initial "stick" phase of bending by prolonging the monolithic behavior, but they do not significantly alter the post-slip stiffness (Fig. 9d and Fig. 9f). The lay angle (α) of the helical wires demonstrated a more complex effect; at small deflections, a larger lay angle results in a more flexible response, but this also delays the transition to the final slip region, causing the curve to cross the baseline and become stiffer at larger deflections (Fig. 9c). Finally, the Poisson's ratio (ν_s) of the signal cable was found to have a negligible effect on the bending stiffness (Fig. 9e).

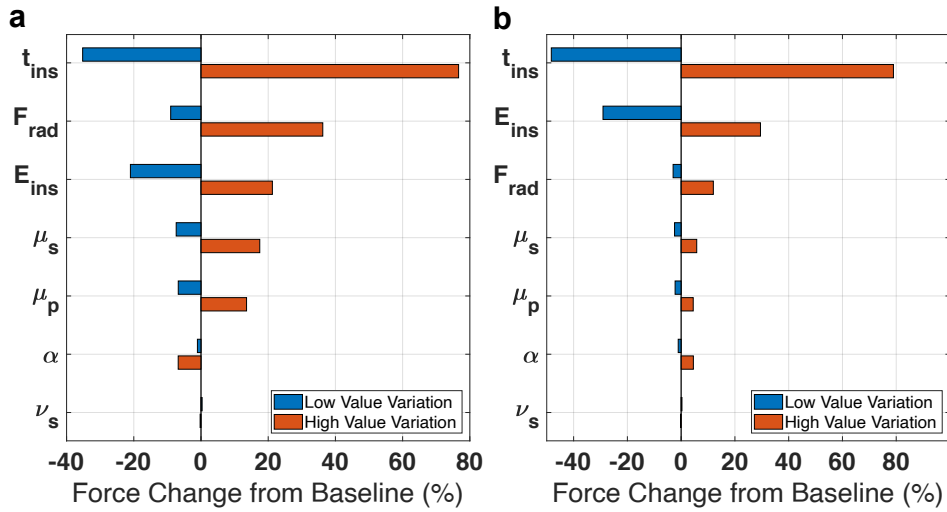


Fig. 10 Tornado plot illustrating the sensitivity of the bending force to changes in key design parameters, evaluated at both **a.** a small (1 mm) and **b.** large (4 mm) deflection. The length of each bar represents the percentage change in force from the baseline when a parameter is varied to its low or high value.

To provide a quantitative ranking, the percentage change in the required bending force from the baseline of each parameter was calculated at two deflections: 1 mm and a larger deflection of 4 mm. The results are visualized in a tornado plot in Fig. 10. This analysis revealed a clear hierarchy of parameter influences that shift with the degree of deformation. At small deflections (Fig. 10a), the insulation thickness (t_{ins}) is the most influential parameter, causing a $\approx 40\%$ decrease and $\approx 80\%$ increase in force at its low and high variations, respectively. It is followed by the radial force (F_{rad}), which causes a $\approx 10\%$ decrease and $\approx 40\%$ increase. At larger deflections (4 mm), the insulation thickness remains the most dominant parameter, but the insulation's Young's modulus (E_{ins}) becomes the second most important factor, surpassing the radial force (Fig. 10b). This shift highlights the different mechanical regimes of the driveline's response: the interfacial properties are critical in governing the initial

“stick” phase, while the bulk material properties, such as E_{ins} , become more dominant in determining the post-slip stiffness. This shift is also reflected in the interfacial friction coefficients (μ_s , μ_p); their combined average percentage effect on force drops from approximately 15% at 1 mm to less than 5% at 4 mm deflection.

As mentioned in Sec. 4.3, this analysis neglects the influence of temperature and axial tension (pre-stress). The model was calibrated using data from experiments at an ambient temperature of 22°C, which differs from the *in vivo* environment of approximately 36.5°C. This temperature differential is expected to alter material properties, particularly decrease the modulus of silicone and PTFE, and therefore reduce the driveline’s bending stiffness [31, 32]. Given that drivelines are implanted with some slack within the body [33], the pre-stressing from implantation is likely to be minimal. While a full thermomechanical characterization was beyond this study’s scope, future work should address these coupled effects. A potential framework for such an analysis is provided by work on large-scale cable structures, where generalized equivalent modulus approaches incorporate both inelastic thermal loads and stress levels into the system’s effective stiffness [31]. This framework could be adapted to model how temperature and pre-stress modify the driveline’s bending stiffness.

Furthermore, while this study focuses on the quasi-static bending stiffness, long-term driveline durability is critically governed by fatigue resistance. In a clinical setting, the driveline is subjected to millions of low-amplitude bending cycles from patient movement. The stick-slip model presented here, while not a fatigue model itself, provides a crucial foundation for such an analysis. The micro-sliding at the material interfaces, which our model quantifies, is the primary mechanism for fretting fatigue. As documented in comprehensive reviews of biomedical cables, repeated interfacial motion involving friction and wear is a key factor in the fatigue response of multi-component systems [34]. Over many cycles, this can lead to material degradation and crack initiation in the conductors, ultimately compromising the driveline’s integrity. A comprehensive fatigue life prediction would require extending the current framework to include a damage accumulation law that accounts for this cyclic micro-sliding. The absence of such a fatigue analysis is therefore a key limitation to be addressed in future work.

A further limitation is the model’s scope, which is confined to the inner core and does not include the outer aramid braiding and silicone coating. As justified in Section 4, this was an intentional approach to first validate the complex mechanics of the inner assembly. Consequently, while the model accurately predicts the core’s behavior, it does not represent the full driveline’s bending response. Our ongoing research is focused on extending this framework to a complete composite model that incorporates the mechanical properties of these outer layers.

With these limitations considered, the sensitivity analysis presented in this section identifies the primary drivers of bending stiffness. The findings can provide a clear and quantitative roadmap for design optimization, as discussed further in Sec. 6.

6 Design recommendations for more flexible drivelines

The presented framework provides clear, model-driven insights for optimizing driveline design. Based on our sensitivity analysis, the most effective strategy for reducing bending stiffness is to decrease the insulation jacket's thickness (t_{ins}) and/or its Young's modulus (E_{ins}). However, this modification must be balanced against the critical need for mechanical durability. A composite design approach is essential for managing this trade-off. The overall strength of the driveline is not solely dependent on the insulation jacket; rather, specific layers are engineered for mechanical integrity. The HM3 design, for example, includes a central polyethylene core braiding that increases the tensile strength of the cable and an outer aramid fiber armor layer that provides robust reinforcement against abrasion and cuts. By designing each layer for a specific job—the insulation for flexibility and the braids for strength and cut resistance—we can make the driveline more flexible while keeping it mechanically durable.

The importance of driveline stiffness is further underscored by animal trial and experimental studies. First, an animal study by [35] proposed recommendations similar to ours for improving patient outcomes. Smaller drivelines with low flexural stiffness exhibited a 34 times lower subcutaneous bacterial load, which is an indicator of DLI (2.5×10^3 CFU/ml vs. 8.5×10^4 CFU/ml) compared to conventional drivelines. Second, the Pellethane and Carbothane versions of the HVAD driveline have the same internal geometry, yet exhibit significantly different bending stiffness values [16]. This difference is attributable to the change in the outer jacketing material. Hence, these material properties should be considered as primary targets for further driveline design improvements.

Another approach is to tune the interfacial properties to control the bending stiffness. Reducing the radial force (F_{rad}) exerted by the jacket can be achieved by optimizing the shrink-fit tubing application during manufacturing to apply less compressive force. Similarly, the friction coefficients can be lowered by design, for example through the inclusion of a low-friction layer like the PTFE sheath already present in the HM3.

When considering these design improvements, the effect of each change on other critical properties—such as cut resistance, electromagnetic interference, tensile strength, heat tolerance, and electrical functionality—must always be included in the optimization loop.

7 Conclusion

We present a comprehensive mechanical analysis of VAD drivelines, motivated by the clinical need for improved mechanical designs to reduce driveline-related infections and improve the cost-effectiveness of VAD therapy. We begin by investigating the design of HVAD and HM3 drivelines in the market. We then design and perform standardized experimental bending tests to obtain the mechanical response of multilayered driveline designs. We demonstrated that the HM3 driveline exhibits a higher effective flexural rigidity than the HVAD driveline. While raw force-deflection data can provide a preliminary comparison, this is further clarified by a rigorous moment-curvature analysis. We then expanded this analysis with a detailed, layer-by-layer deconstruction of the

HM3 driveline. We performed dedicated bending experiments for each subsequent layers. This approach provided definitive evidence of its complex, non-additive composite behavior and highlighted the critical role of inter-component friction and slip.

We develop a physics-based mathematical model for further mathematical analysis. The mathematical framework from the literature is implemented and calibrated using the experimental findings for the single 30 AWG cable and the 7-wire helically stranded cable with its insulation jacketing. This calibrated model then enabled a quantitative sensitivity analysis to reveal the effect of each design parameter. This analysis identified the insulation jacket's thickness and material modulus as the most influential parameters governing the driveline's bending stiffness, while also revealing the important role of interfacial forces in the small-deflection regime. Lastly, a clear set of mechanical design principles for the next generation of drivelines is proposed. We suggest that thinner insulation jacketing made of a material with low elasticity modulus and fine-tuned interfacial forces can yield more flexible drivelines with less bending stiffness. These modifications could improve overall mechanical performance of percutaneous drivelines for more successful clinical applications for heart failure patients by lowering the incidence of driveline-related failures and infections.

For future work, the validated modeling framework presented in this paper can be expanded to incorporate axial and torsional loading, as well as to perform multiphysical analysis for the design of multilayered drivelines that consider electrical, thermal, and biological features. For more accurate estimation of mechanical properties, advanced data assimilation techniques can be implemented using the experimental data. Further clinical input is needed for improved overall VAD system performance (e.g., dressing frequency of skin exit site).

Declarations

Conflict of interest/Competing interests

The authors declare no competing interests.

Ethics declarations

The authors declare that they do not have any financial or personal relationships with other people or organisations.

Data availability

The force-displacement data can be provided upon reasonable request.

Code availability

The implemented solver can be provided upon reasonable request.

Declaration of generative AI and AI-assisted technologies in the writing process

Authors clarify the use of large language models for grammar checking and typos.

Appendix A DLI data

We correlated the available structural properties of drivelines with the DLI rate. To do this, we ran a weighted linear regression analysis and used total diameter and bending stiffness as predictors. We present the tabulated DLI data in Table A1 taken from [16]. The sample size for each data point is included to improve the accuracy of the weights for each parameter. The weighted least squares (WLS) regression analysis was set to have an intercept of zero. The calculated squared error is $R^2 = 0.863$. The diameter showed stronger influence ($p < 0.001$) than bending stiffness ($p < 0.003$), agreeing with [15]. The qualitative interpretation of our findings agrees with [15], suggesting thinner drivelines for reduced DLI rates. This may be because the chance of bacterial movement may be less for thinner drivelines due to the smaller contact surface area [36]. Furthermore, a stiffer driveline design contributes to the DLI rate as well, per the regression study. Qualitatively, Imamura et. al. reached the same conclusion, noting that the stiffer drivelines may cause more torque at the skin exit site [15]. This may be due to the disintegration at the driveline–integument interface, and may eventually may cause further trauma [37].

References

- [1] Gude, E., Fiane, A.E.: Can mechanical circulatory support be an effective treatment for hfpef patients? *Heart Failure Reviews* **28**(2), 297–305 (2023) <https://doi.org/10.1007/s10741-021-10154-1>
- [2] Han, J., Trumble, D.R.: Cardiac assist devices: early concepts, current technologies, and future innovations. *Bioengineering* **6**(1), 18 (2019) <https://doi.org/10.3390/bioengineering6010018>
- [3] Campi, T., Cruciani, S., Maradei, F., Montaldo, A., Musumeci, F., Feliziani, M.: Thermal analysis of a transcutaneous energy transfer system for a left ventricular assist device. *IEEE Journal of Electromagnetics, RF and Microwaves in Medicine and Biology* **6**(2), 253–259 (2021) <https://doi.org/10.1109/JERM.2021.3109449>
- [4] Pya, Y., Maly, J., Bekbossynova, M., Salov, R., Schueler, S., Meyns, B., Kassif, Y., Massetti, M., Zilberslag, M., Netuka, I.: First human use of a wireless coplanar energy transfer coupled with a continuous-flow left ventricular assist device. *The Journal of Heart and Lung Transplantation* **38**(4), 339–343 (2019) <https://doi.org/10.1016/j.healun.2019.01.1316>
- [5] Potapov, E.V., Kaufmann, F., Stepanenko, A., Hening, E., Vierecke, J., Löw, A., Lehmkuhl, E., Dranishnikov, N., Hetzer, R., Krabatsch, T.: Pump exchange for cable damage in patients supported with heartmate ii left ventricular assist device. *ASAIO Journal* **58**(6), 578–582 (2012) <https://doi.org/10.1097/MAT.0b013e3182703718>
- [6] Pavlovic, N.V., Randell, T., Madeira, T., Hsu, S., Zinoviev, R., Abshire, M.: Risk of left ventricular assist device driveline infection: A systematic literature review.

Table A1 Data taken from [16] to obtain regression framework.

Device	Diameter (mm)	Bending Stiffness (N)	Infection Rate (%)	Sample Size
HVAD	4.8	15.55	3.6	171
			13.5	111
			14.2	305
			9.0	56
			11.0	382
			3.3	26
			9.0	44
			2.9	80
			9.1	79
			12.0	41
HMII	6.0	4.52	8.3	23
			4.9	560
			6.0	285
			7.0	50
			9.6	43
			4.0	71
			15.7	17
			14.2	66
			11.4	194
			7.2	278
			4.0	32
			7.0	2006
			10.4	82
			29.0	31
HM3	6.0	11.08	14.3	7
			10.0	50
			27.6	29
			6.8	56
			10.0	50

Heart and Lung **48**(2), 90–104 (2019) <https://doi.org/10.1016/j.hrtlng.2018.11.002>

- [7] D'Antonio, N.D., Maynes, E.J., Tatum, R.T., Prochno, K.W., Saxena, A., Maltais, S., Samuels, L.E., Morris, R.J., Massey, H.T., Tchantchaleishvili, V.: Driveline damage and repair in continuous-flow left ventricular assist devices: A systematic review. Artificial Organs **45**(8), 819–826 (2021) <https://doi.org/10.1111/aor.13901>
- [8] Kalavrouziotis, D., Tong, M.Z., Starling, R.C., Massiello, A., Soltesz, E., Smedira, N.G., Fryc, R., Heatley, G., Farrar, D.J., Moazami, N.: Percutaneous lead dysfunction in the heartmate ii left ventricular assist device. The Annals of thoracic surgery **97**(4), 1373–1378 (2014) <https://doi.org/10.1016/j.athoracsur.2013.11.039>
- [9] Ilias Basha, H., Givens, R.C., Cagliostro, B., Parkins, G., Flannery, M., Te-Frey,

- R., Garan, A.R., Yuzefpolskaya, M., Takayama, H., Takeda, K., Naka, Y., Farr, M.A., Colombo, P.C., Topkara, V.K.: (1308) - the short-to-shield phenomenon in heartmate ii left ventricular assist devices: A single center experience. *The Journal of Heart and Lung Transplantation* **36**(4, Supplement), 426–427 (2017) <https://doi.org/10.1016/j.healun.2017.01.1220>
- [10] Matsumoto, Y., Fukushima, S., Shimahara, Y., Yamashita, K., Kawamoto, N., Kuroda, K., Seguchi, O., Yanase, M., Fukushima, N., Shimizu, H., *et al.*: Driveline angle is crucial for preventing driveline infection in patients with heartmate ii device. *Journal of Artificial Organs* **22**, 37–43 (2019) <https://doi.org/10.1007/s10047-018-1074-x>
 - [11] Hernandez, G.A., Nunez Breton, J.D., Chaparro, S.V.: Driveline infection in ventricular assist devices and its implication in the present era of destination therapy. *Open journal of cardiovascular surgery* **9**, 1179065217714216 (2017) <https://doi.org/10.1177/1179065217714216>
 - [12] Soltani, S., Kaufmann, F., Vierecke, J., Kretzschmar, A., Hennig, E., Stein, J., Hetzer, R., Krabatsch, T., Potapov, E.V.: Design changes in continuous-flow left ventricular assist devices and life-threatening pump malfunctions. *European Journal of Cardio-Thoracic Surgery* **47**(6), 984–989 (2015) <https://doi.org/10.1093/ejcts/ezu347>
 - [13] Miller, L.W., Guglin, M., Rogers, J.: Cost of ventricular assist devices: can we afford the progress? *Circulation* **127**(6), 743–748 (2013) <https://doi.org/10.1161/CIRCULATIONAHA.112.139824>
 - [14] Schmier, J.K., Patel, J.D., Leonhard, M.J., Midha, P.A.: A systematic review of cost-effectiveness analyses of left ventricular assist devices: issues and challenges. *Applied health economics and health policy* **17**(1), 35–46 (2019) <https://doi.org/10.1007/s40258-018-0439-x>
 - [15] Imamura, T., Murasawa, T., Kawasaki, H., Kashiwa, K., Kinoshita, O., Nawata, K., Ono, M.: Correlation between driveline features and driveline infection in left ventricular assist device selection. *Journal of Artificial Organs* **20**, 34–41 (2017) <https://doi.org/10.1007/s10047-016-0923-8>
 - [16] Kranzl, M., Stoiber, M., Schaefer, A.-K., Riebandt, J., Wiedemann, D., Marko, C., Laufer, G., Zimpfer, D., Schima, H., Schlöglhofer, T.: Driveline features as risk factor for infection in left ventricular assist devices: meta-analysis and experimental tests. *Frontiers in Cardiovascular Medicine* **8**, 784208 (2021) <https://doi.org/10.3389/fcvm.2021.784208>
 - [17] Matsumoto, Y., Fujita, T., Fukushima, S., Hata, H., Shimahara, Y., Kume, Y., Yamashita, K., Kuroda, K., Nakajima, S., Sunami, H., *et al.*: 889 days of support on hydrodynamic bearing rotation mode of the duraheart™ for bridge-to-heart transplantation. *Journal of Artificial Organs* **20**, 270–273 (2017) <https://doi.org/>

[10.1007/s10047-017-0962-9](https://doi.org/10.1007/s10047-017-0962-9)

- [18] Schläglhofer, T., Michalovics, P., Riebandt, J., Angleitner, P., Stoiber, M., Laufer, G., Schima, H., Wiedemann, D., Zimpfer, D., Moscato, F.: Left ventricular assist device driveline infections in three contemporary devices. *Artificial Organs* **45**(5), 464–472 (2021) <https://doi.org/10.1111/aor.13843>
- [19] Qu, Y., McGiffin, D., Sanchez, L.D., Gengenbach, T., Easton, C., Thissen, H., Peleg, A.Y.: Anti-infective characteristics of a new carbothane ventricular assist device driveline. *Biofilm* **5**, 100124 (2023) <https://doi.org/10.1016/j.bioflm.2023.100124>
- [20] Merzah, A.S., Hanke, J.S., Li, T., Saad Merzah, F.A., Gabriel, M., Derda, A.A., Homann, K., Haverich, A., Schmitto, J.D., Dogan, G.: Outcomes of modular cable exchange in heartmate 3 patients versus conventional driveline repair in heartmate ii patients. *Artificial Organs* **47**(2), 380–386 (2023) <https://doi.org/10.1111/aor.14413>
- [21] International Organization for Standardization: Plastics — Determination of flexural properties. <https://www.iso.org/standard/70513.html>, Geneva, Switzerland. ISO 178:2019 (2019)
- [22] Gaziano, P., Monaldo, E., Falcinelli, C., Vairo, G.: Elasto-damage mechanics of osteons: a bottom-up multiscale approach. *Journal of the Mechanics and Physics of Solids* **167**, 104962 (2022) <https://doi.org/10.1016/j.jmps.2022.104962>
- [23] Zoboli, L., Corte, A., Vairo, G.: Multiscale structural assessment of toroidal field coils via reduced-order models. *Fusion Engineering and Design* **182**, 113216 (2022) <https://doi.org/10.1016/j.fusengdes.2022.113216>
- [24] Vemula, S.S., Ji, M., Headings, L.M., Gargesh, K., Soghrati, S., Dapino, M.J.: Analytical model for large deflection bending of helically stranded electrical wires. *International Journal of Mechanical Sciences* **170**, 105355 (2020) <https://doi.org/10.1016/j.ijmecsci.2019.105355>
- [25] Taghipour, E., Vemula, S.S., Wang, Z., Zhou, Y., Qarib, H., Gargesh, K., Headings, L.M., Dapino, M.J., Soghrati, S.: Characterization and computational modeling of electrical wires and wire bundles subject to bending loads. *International Journal of Mechanical Sciences* **140**, 211–227 (2018) <https://doi.org/10.1016/j.ijmecsci.2018.03.009>
- [26] Taghipour, E., Vemula, S.S., Gargesh, K., Headings, L.M., Dapino, M.J., Soghrati, S.: Finite element analysis of mechanical behavior of electrical wire harnesses: High fidelity and reduced-order models. *International Journal of Mechanical Sciences* **165**, 105188 (2020) <https://doi.org/10.1016/j.ijmecsci.2019.105188>

- [27] Hong, K.-J., Der Kiureghian, A., Sackman, J.L.: Bending behavior of helically wrapped cables. *Journal of engineering mechanics* **131**(5), 500–511 (2005) [https://doi.org/10.1061/\(ASCE\)0733-9399\(2005\)131:5\(500\)](https://doi.org/10.1061/(ASCE)0733-9399(2005)131:5(500))
- [28] Yu, Y., Wang, X., Chen, Z.: A simplified finite element model for structural cable bending mechanism. *International Journal of Mechanical Sciences* **113**, 196–210 (2016) <https://doi.org/10.1016/j.ijmecsci.2016.05.004>
- [29] Cardou, A., Jolicœur, C.: Mechanical models of helical strands. *Applied Mechanics Reviews* **50**(1), 1–14 (1997) <https://doi.org/10.1115/1.3101684>
- [30] Inagaki, K., Ekh, J., Zahrai, S.: Mechanical analysis of second order helical structure in electrical cable. *International journal of solids and structures* **44**(5), 1657–1679 (2007) <https://doi.org/10.1016/j.ijsolstr.2006.06.045>
- [31] Vairo, G., Montassar, S.: In: Frémond, M., Maceri, F. (eds.) *Mechanical Modelling of Stays under Thermal Loads*, pp. 481–498. Springer, Berlin, Heidelberg (2012). https://doi.org/10.1007/978-3-642-24638-8_34
- [32] Montassar, S., Mekki, O.B., Vairo, G.: On the effects of uniform temperature variations on stay cables. *Journal of Civil Structural Health Monitoring* **5**(5), 735–742 (2015) <https://doi.org/10.1007/s13349-015-0140-9>
- [33] Bielecka-Dabrowa, A., Banach, M., Rysz, J., O'Driscoll, G.: Ventricular Assist Device – How to Obtain Optimal Benefits? IntechOpen, London (2011). Chap. 4. <https://doi.org/10.5772/15384>
- [34] Gbur, J.L., Lewandowski, J.J.: Fatigue and fracture of wires and cables for biomedical applications. *International Materials Reviews* **61**(4), 231–314 (2016) <https://doi.org/10.1080/09506608.2016.1152347>
- [35] Kourouklis, A.P., Wu, X., Kaemmel, J., Hertegonne, S., Shambat, S.M., Lee, M., Grossmann, C., Hagen, R., Fehr, D., Spano, F., *et al.*: Reducing driveline infection risk in durable mechanical circulatory systems with ultra-flexible wires for energy transfer. *The Journal of Heart and Lung Transplantation* (2025) <https://doi.org/10.1016/j.healun.2025.07.012>
- [36] Haglund, N.A., Davis, M.E., Tricarico, N.M., Keebler, M.E., Maltais, S.: Readmissions after continuous flow left ventricular assist device implantation: differences observed between two contemporary device types. *ASAIO Journal* **61**(4), 410–416 (2015) <https://doi.org/10.1097/MAT.0000000000000218>
- [37] Goldstein, D.J., Naftel, D., Holman, W., Bellumkonda, L., Pamboukian, S.V., Pagani, F.D., Kirklin, J.: Continuous-flow devices and percutaneous site infections: clinical outcomes. *The Journal of heart and lung transplantation* **31**(11), 1151–1157 (2012) <https://doi.org/10.1016/j.healun.2012.05.004>